Imaging Ultrafast Dynamics of Pressure-Driven Phase Transitions in Black Phosphorus and Anomalous Coherent Phonon Softening

Simin Wu,[¶] Weibin Chu,[*,¶] Yang Lu,[*] and Minbiao Ji[*]

Read Online

ACCESS | Metrics & More | Article Recommendations | Supporting Information

ABSTRACT: Applying high pressure to effectively modulate the electronic and lattice structures of materials could unravel various physical properties associated with phase transitions. In this work, high-pressure-compatible femtosecond pump−probe microscopy was constructed to study the pressure-dependent ultrafast dynamics in black phosphorus (BP) thin films. We observed pressure-driven evolution of the electronic topological transition and three structural phases as the pressure reached ∼22 GPa, which could be clearly differentiated in the transient absorption images containing spatially resolved ultrafast carrier and coherent phonon dynamics. Surprisingly, an anomalous coherent acoustic phonon mode with pressure softening behavior was observed within the range of ∼3−8 GPa, showing distinct laser power and time dependences. Density functional theory calculations show that this mode, identified as the shear mode along the armchair orientation, gains significant electron−phonon coupling strength from out-of-plane compression that leads to decreased phonon frequency. Our results provide insights into the structure evolution of BP with pressure and hold potential for applications in microelectromechanical devices.

KEYWORDS: Black phosphorus, high pressure, coherent phonon, pump−probe microscopy, ultrafast dynamics, phase transition
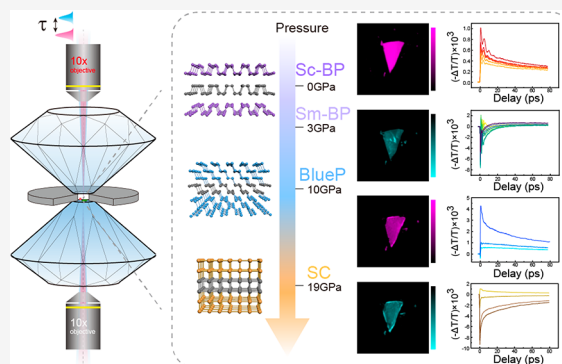
As a unique two-dimensional (2D) semiconductor material, black phosphorus (BP) has attracted growing research interest in recent years, exhibiting a number of remarkable physical properties. These include thickness-tunable direct bandgaps from 0.35 ev (bulk) to 1.7 ev (monolayer),[1,2] excitonic transitions of both linear and transient optical responses,[1−3] in-plane optical and mechanical anisotropies due to puckered orthorhombic layered structure,[4,5] and exotic electronic properties,[6,7] which have proven BP as a promising candidate for future optoelectronic devices. In addition to the intrinsic pristine properties, BP has also demonstrated interesting responses to external modulations, such as electric tuning, mechanical tuning, vertical stacking and Moiré patterning.[8−12]

Pressure is another important parameter that could be externally applied to change lattice constants and induce phase transitions for 2D materials,[13,14] hence effectively modulating the interlayer coupling and altering the optical and electronic properties. For instance, pressure-induced metallization and superconductivity have been observed in BP, transition metal dichalcogenide (TMDC) and 2D magnetic materials;[15−17] bandgap opening occurs in trilayer graphene under high pressure,[18] and insulator to metal transition in VO_2.[19,20] Compared with the traditional mechanical bending/stretching methods with small in-plane strains of less than 4%, diamond-anvil cell (DAC) can readily exert high pressures up to hundreds of GPa and yield compressive out-of-plane strain as

high as 30%,[21] making the DAC technique a powerful tool to study 2D materials under extreme pressure conditions. Previous studies have revealed a topological semiconductor-to-metal electronic transition at ∼1.2 GPa on bulk BP crystal with thickness much larger than 1 μm.[22] Raman and XRD studies have revealed pressure-induced phase transitions from black phosphorus (orthorhombic BP phase, A17 structure) to blue phosphorus (rhombohedral BlueP phase, A7 structure) and further to simple cubic (SC phase) with increasing pressures.[15,23−25] It is also found that the critical pressures of BP phase transitions are thickness-dependent, with thinner films requiring higher transition pressures.[26] On the one hand, recent studies of the linear and static optical spectroscopy of BP under high pressures have shown rich information on phase transition and band structure evolution.[15,22,27] On the other hand, ultrafast optical spectroscopy of BP under normal pressure demonstrated properties including altered excitonic resonance induced by excited photocarriers, layer-dependent coherent phonon (CP) dynamics,[3,28] and dichroic photo-
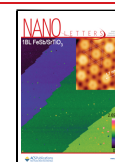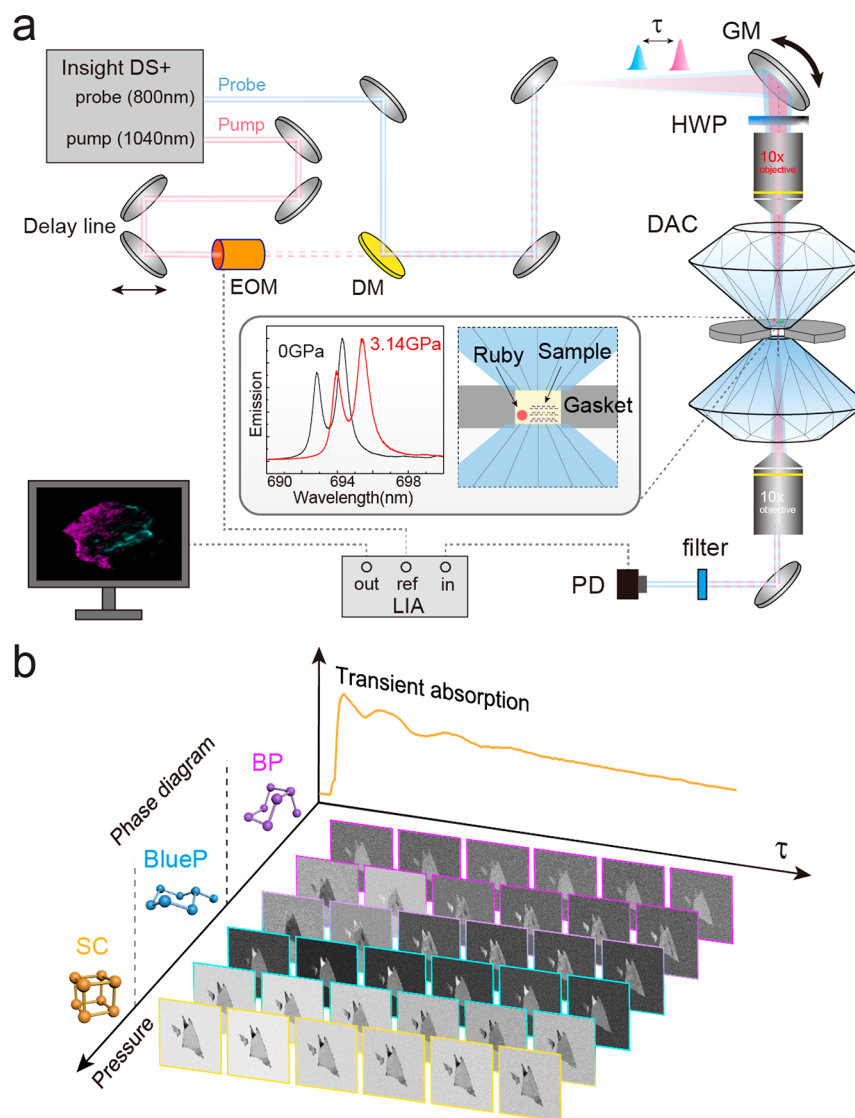
Figure 1. High-pressure compatible femtosecond pump−probe microscopy to study phase transitions of black phosphorus. (a) Schematic illustration of the pump−probe microscope coupled with diamond anvil cell (DAC). EOM: electro-optical modulator; DM: dichroic mirror; GM: galvo mirror; HWP: half-wave plate; PD: photo diode; LIA: lock-in amplifier. (b) Transient absorption (TA) images taken at varying delay times (τ) and pressures, with different phases shown in the diagram. BP: black phosphorus; BlueP: blue phosphorus; SC: simple cubic phase.

elasticity.[29] However, the ultrafast transient behaviors of BP associated with pressure-induced phase transitions remain elusive.

Femtosecond pump−probe microscopy has been developed to obtain transient absorption (TA) dynamics with high speed, high temporal and spatial resolutions.[30] Compared with conventional pump−probe spectroscopy with fixed laser spot, TA imaging utilizes rapid laser scanning technique with reduced photodamage and allows high-throughput measurements on small-size heterogeneous specimens. Therefore, pump−probe microscopy has demonstrated unique applications in material science,[3,29] biomedical imaging[31−33] and archeological research.[34] Applying such a technique to study materials under extreme pressure conditions provides transient properties of the nonequilibrium excited states at different phases.

In this work, we built a high-pressure-compatible femtosecond pump−probe microscopy to investigate the ultrafast dynamics of BP in situ under the pressure range of 0−22 GPa.

BP flakes (∼20 nm thickness) demonstrated transitions from orthorhombic to rhombohedral phase at ∼10 GPa, and simple cubic phase at ∼19 GPa, with characteristic transient photocarrier and CP behaviors for each phase. Spatial heterogeneities showing the coexistence of different transient behaviors within single fakes were observed in the intermediate states. The photoexcited carriers experienced switching signs of transient absorption signals during phase transitions. More-over, CP dynamics exhibited phase-dependent responses to pressure, excitation power, and relaxation time. An anomalous phonon mode was observed in the semimetal phase with pressure softening behavior under increased pressures, demonstrating an exotic frequency response to photocarrier density. These imply giant electron−phonon coupling (EPC) for the intermediate semimetal phase as verified by our calculations.

We first built a high-pressure-compatible femtosecond pump−probe microscope coupled with a diamond-anvil cell to measure the ultrafast dynamics of samples in situ
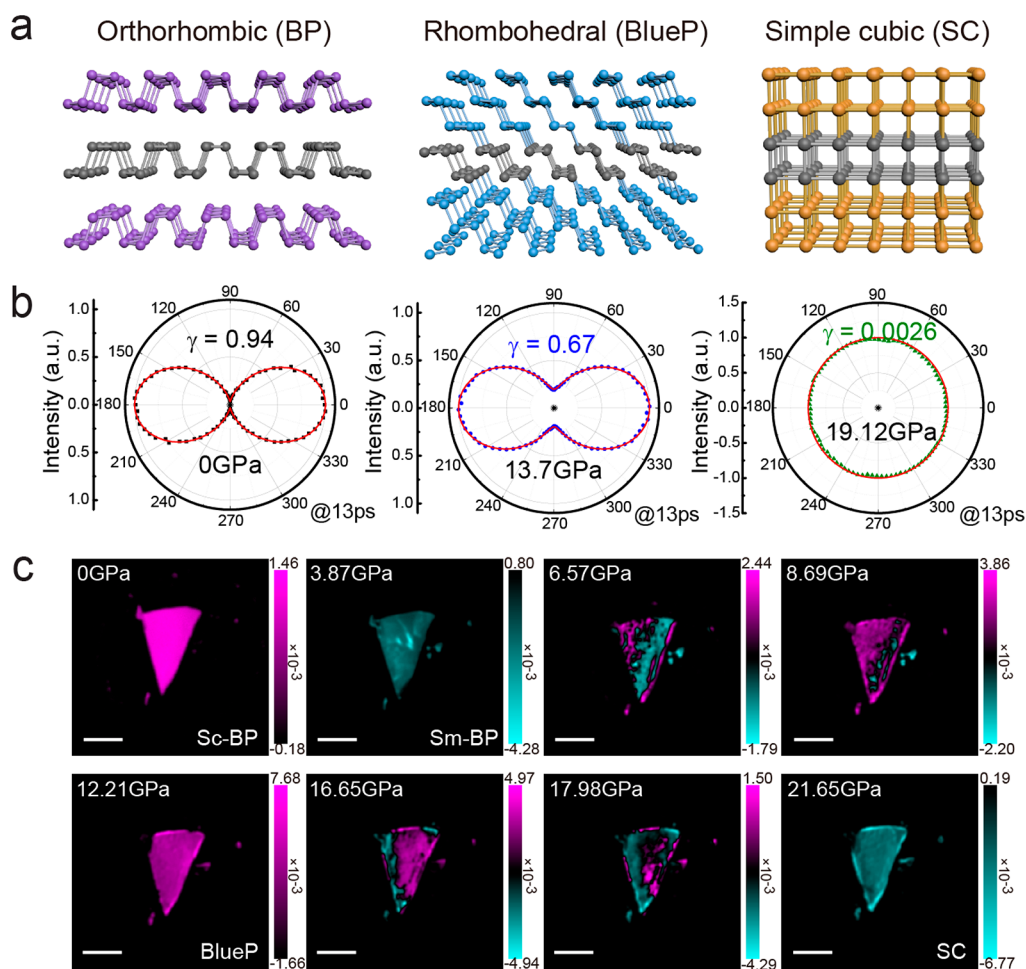
Figure 2. Characterizing high-pressure phases of BP with polarization-resolved pump−probe imaging. (a) Crystal structures of orthorhombic (BP), rhombohedral (BlueP), and simple cubic (SC) phases. (b) Polarization dependence of TA intensity (τ = 13 ps) reveals anisotropy differences among the three phases. (c) TA images of a typical BP flake under varying pressures from 0 GPa to ∼22 GPa. Sc-BP: semiconductor BP; Sm-BP: semimetal BP. Scale bars: 10 μm.

(Supporting Information and Figure 1a). The laser-scanning microscope system is capable of imaging transient optical signals with decent temporal resolution (∼200 fs) and spatial resolution (∼1.3 μm, 10× objective with NA = 0.3) as characterized in Figure S1. With a fixed 1040 nm pump and an 800 nm probe (tuning range of 700−940 nm in wavelength-dependence measurements), we detected the TA signal as the differential absorbance ($S = -\Delta T/T$) of the probe beam induced by the modulated pump beam and generated images as the focused laser spot raster scanned across the sample with a pixel dwell time of ∼2 μs and a frame rate of ∼1 fps (512 × 512 pixels). To investigate the anisotropic properties of BP, the parallelly aligned polarizations of both beams were controlled by a motorized half-wave plate to measure the polarization-resolved signal $S(\theta)$. The polarization response of our microscope system was optimized and calibrated using isotropic samples such as graphite flakes in DAC (Figure S2). By variation of the time delay (τ) between the pump and probe pulses for each image frame, an image stack $S(x, y, \tau, \theta)$ could be generated to provide region-resolved transient dynamics of the inhomogeneous sample under varying pressures (Figure 1b). The nanoscale BP flakes were mechanically exfoliated on polydimethylsiloxane (PDMS) and then transferred onto the diamond surface of the DAC. Silicone oil in the DAC was used as an inert pressure

transmitting medium (PTM) and was verified to cause a minimum effect on BP transient dynamics compared with a bare sample (Figure S3). The pressure in DAC was characterized by measuring the photoluminescence emission spectra of a ruby bead placed in close proximity to the sample,[35,36] as shown in the inset of Figure 1a. The stress on the sample can be approximated as uniaxial considering the nanoscale thickness of BP films and the adhesion effect to the substrate.[27]

As a BP flake is exerted by increasing pressure, it experiences three phases with distinct crystal structures (Figure 2a). At ambient conditions, the layered semiconducting orthorhombic phase is the thermodynamically stable allotrope of the phosphorus element. For a measured flake with ∼20 nm thickness, it undergoes a phase transition to a layered semimetallic rhombohedral BlueP phase at ∼10 GPa, and further transforms to a metallic simple-cubic phase at ∼19 GPa. These structural evolutions of BP during phase transitions could also be reflected in the anisotropy of pump−probe measurements. Polarization-resolved TA signal $S(\theta, \tau = 13\ \text{ps})$ demonstrated different angular patterns for the three phases (Figure 2b), with θ = 0 and 90 corresponding to the armchair (AC) and zigzag (ZZ) orientations, respectively. We found the largest anisotropy (γ, defined in Supporting Information) in the BP phase (γ = 0.94), decreased anisotropy
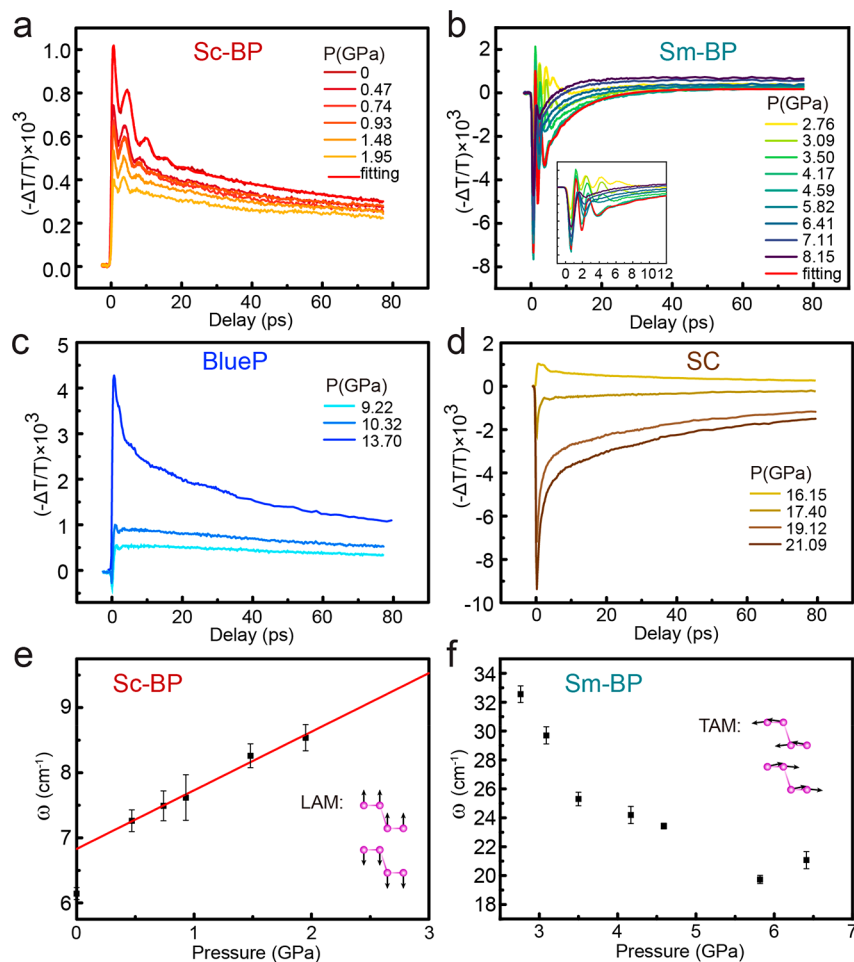
Figure 3. Pressure-dependent ultrafast dynamics of BP under different phases. (a) Photoinduced absorption curves in Sc-BP phase under 0−3 GPa. (b) Photoinduced bleaching curves in Sm-BP phase under 3−8 GPa. (c) Photoinduced absorption curves in BlueP phase under 9−13 GPa. (d) Photoinduced bleaching curves in SC phase under 16−21 GPa. (e) Pressure induced stiffening of the longitudinal acoustic mode (LAM) phonon in Sc-BP phase. (f) Pressure induced softening of transverse acoustic mode (TAM) phonon in Sm-BP phase.

in the BlueP phase ($\gamma = 0.67$), and almost complete loss of anisotropy in the sc phase ($\gamma = 0.0026$), which agreed with the trend of structural transitions.

The process of pressure-induced phase transitions on a single flake could be clearly visualized in the pump−probe images $S(x, y, \tau = 1.5$ ps$, \theta = 0)$ taken in the AC direction and under various pressures within the range of 0−22 GPa (Figure 2c). We color-coded the positive TA (photoinduced absorption, PA) signals in magenta and the negative (photoinduced bleach, PB) signals in cyan. The pump−probe images readily demonstrated detailed information on evolving TA signals and their spatial distributions during phase transitions. First of all, the changing sign of TA signal reflects the electronic and structural phase evolution during the course of pressure rise (Figure 2c and Movie S1). The initial positive PA signal in the BP phase quickly decreased and turned into negative PB signal at ∼3 GPa, indicating that the out-of-plane compressive strain reduced the imaginary refractive index along AC direction, echoing with previous results.[29] The persistent spatially homogeneous TA images indicated that no structural transition occurred within this pressure range (0−6 GPa). Instead, it could be attributed to the electronic transition from semiconductor-BP (Sc-BP) to semimetal-BP (Sm-BP) state.[22] As the pressure exceeded 6 GPa, the transient signal switched to positive PA from the edges of the flake,

which was regarded as the structural transition to the rhombohedral BlueP phase. The spatially inhomogeneous images showed the coexistence of BP and BlueP phases with increasing BlueP areas under higher pressures, and gradually became uniform at ∼12 GPa, indicating complete transformation of the whole flake. Similarly, at higher pressures, the BlueP crystal phase started to partially transform from the edges, where the TA signal switched to negative PB again, which was attributed to the SC phase. After experiencing another intermediate mixed state, the crystal thoroughly transformed into a uniform SC phase at ∼19 GPa. The high spatial resolution of pump−probe microscopy enables the observation of region-dependent responses of a single crystal to external pressure, which may indicate significant internal strain across the sample during structural phase transitions, while the electronic transition appears relatively homogeneous without the abrupt change in lattice structure. Our results demonstrated an electronic phase transition from semiconductor to semimetal at around 3 GPa and two structural transition pressures at around 10 GPa (Sm-BP to BlueP) and 19 GPa (BlueP to SC) in a BP flake (∼20 nm thick), which was consistent with XRD study.[26] Our measured Raman spectra from 0 to 22 GPa also provided evidence of three phase transitions (Figure S4).

The time-resolved transient dynamics was extracted as $S(\tau)$ by integrating the signals within each region of interest (ROI) of the sample measured in the AC direction, $S(\tau) = \iint_{x,y \in D} S(x,y,\tau,\theta = 0)dxdy$. Representative transient responses of BP flake (~20 nm thick) under different pressures are shown in Figure 3a−d. As the pressure increases, the overall features of the transient dynamics associated with phase transitions can be readily observed. Consistent with the imaging results (Figure 2c), the switching signs of pump−probe signal between positive PA and negative PB occurred three times throughout the transition processes from BP to SC phases, implying pressure-induced changes of electronic band structures. The PA signal was mainly attributed to the excited-state-absorption (ESA) of intraband transition of the excited photocarriers, whereas the PB signal was attributed to the ground-state-bleaching (GSB) and Pauli blocking of the interband transition.

Detailed transient behaviors of photocarrier and coherent-phonon (CP) change remarkably in response to high pressures, including carrier lifetime, CP frequency, etc. To quantify the transient dynamics associated with the many-body interaction processes, we fitted the relaxation curve with a triexponential decay function superposed to a damped oscillation term

$$S(t) = \sum_{n=1,2,3} \left(A_n \exp\left(-\frac{t}{\tau_n}\right) \right), \text{ where } A_n \text{ and } \tau_n \ (n = $$

$$+ B\exp\left(-\frac{t}{\tau_{ph}}\right)\cos(\omega t + \varphi)$$

1,2,3) denote the amplitude and relaxation lifetimes of three different photocarrier contributions; B, τ_{ph}, ω and φ correspond to the amplitude, damping time, oscillation frequency and phase of the coherent phonon. Photocarriers usually experience multiple relaxation processes of different time scales, including the initial formation of quasi-Fermi Dirac (QFD) distribution within 10−50 fs via electron−electron (e−e) scattering, followed by thermalization through electron−phonon (e-ph) scattering at several ps time scale, as well as phonon−phonon (ph-ph) scattering at tens of ps time scale; and finally relax to the ground state via interband electron−hole (e-h) recombination at hundreds of ps time scale.[37,38] In our analysis, we attributed the first component (A_1, τ_1) to the electron−phonon scattering after photoexcitation, the second component (A_2, τ_2) to phonon−phonon scattering, and the third component (A_3, τ_3) to the interband electron−hole recombination. The carrier relaxation processes under different pressures are parametrized and summarized in Table 1, revealing the varying contributions of these transient processes among different phases.

Coherent phonon contributions extracted from the transient dynamics exhibited significant pressure- and phase-dependences. While very weak CP signatures were shown in the BlueP and sc phases, strong CP oscillations could be observed in the BP phase, both in the low-pressure semiconductor phase (0−3 GPa) and higher-pressure (3−8 GPa) semimetal phase. The two electronic phases demonstrate distinct properties in response to pressure and laser power density as well as dynamic temporal evolution. In the Sc-BP phase, longitudinal acoustic mode phonon (LAM), i.e. layer-breathing mode dominates the transient optical signal.[3,29] Whereas in the Sm-BP phase, coherent transverse acoustic mode (TAM) phonon, i.e., shear mode, takes over, whose unique behavior will be carefully analyzed in the next section. The measured pressure-dependent phonon frequencies of the Sc- and Sm-BP are shown in Figure 3ef, respectively. The phonon frequency of LBM shows a linear dependence on pressure, with higher pressure inducing blue-shifted frequency. The pressure hardening of the out-of-plane vibration could be analyzed as $\frac{\partial \omega}{\partial p} \sim$ 0.9 cm^{-1}/GPa, which could be used to further calculate the Grüneisen parameter $\gamma_0 = \frac{B_0}{\omega_0}\frac{\partial \omega}{\partial p} \sim 4.74$, where $B_0 = 36$ GPa represents bulk modulus. As studied in our previous works, the layer-number (N)-dependent frequency of longitudinal acoustic phonon could be explained by the linear (1D) chain model,[3,29,39,40] with $\omega_N = \sqrt{\frac{\beta_B}{2\mu\pi^2c^2}\left(1 - \cos\frac{\pi}{N}\right)}$. To qualitatively understand the phonon hardening effect, it can be seen that longitudinal compressive strain reduces the lattice constant and increases the force constant β_B.[14,41] In addition, both the phonon oscillation amplitude (B) and damping time (τ_{ph}) were found to decrease with increasing pressure until the occurrence of the transition to Sm-BP phase (Figure S5).

As BP transforms to the semimetal phase under higher pressure (3−8 GPa), another dominating acoustic phonon mode was discovered that showed anomalous properties compared with the LAM in the Sc-BP. First of all, the phonon frequency of Sm-BP showed weak dependence on sample thickness, in contrast to the strong thickness-dependent LAM in Sc-BP, as shown in the results of a flake with two regions of different thicknesses (~20 and ~15 nm in Figure 4a), as well as in another ~9 nm thick sample (Figure S6). Regardless of the thickness, the CP frequency of the semimetal phase was measured to be ~25 cm^{-1} under ~4 GPa. Second, a phonon softening phenomena with increasing pressure was found in the semimetal phase, opposite to the common phonon hardening seen in the semiconductor phase (Figure 3e,f). In addition, time-domain phonon softening was observed (Figure 4b), showing slower phonon oscillations as the photoexcited carriers relaxed. Such "phonon-chirping" could be characterized as $\omega_\tau = \omega_0 - \alpha\tau$, and used to fit the phonon dynamics to extract $\omega_0 = 31$ cm^{-1} and $\alpha = 1.4$ cm^{-1}/ps. Furthermore, photocarrier-induced hardening was demonstrated by laser power-dependent measurements. The phonon frequency showed a linear blue-shift with increasing pump (excitation) power (Figure 4c,d), while it appeared independent of the probe (detection) power and wavelength (Figure 4e,f and Figure S7). Such dependence of phonon frequency on photocarrier density matches well with the time-domain results.

We attribute this peculiar phonon mode to the TAM phonon based on the above results of thickness-, pressure-, and time-dependences. The phonon frequency could be explained by the shear mode (C mode) lattice vibration under 1D chain model, $\omega_N = \sqrt{\frac{\beta_C}{2\mu\pi^2c^2}\left(1 + \cos\frac{\pi}{N}\right)}$, showing weak layer

Table 1. Normalized Carrier Relaxation Dynamics of BP Film in the Four States Fitted by Triexponential Decay Function

Phase	Signal type	A_1	τ_1/ps	A_2	τ_2/ps	A_3	τ_3/ps
SC-BP	PA	0.32	4.64	0.10	37.84	**0.58**	598.55
SM-BP	PB	**0.82**	4.94	0.29	17.68	−0.11	443.44
bP	PA	0.44	3.12	0.09	39.37	**0.47**	253.22
sc	PB	**0.54**	1.33	0.10	15.07	0.36	208.97
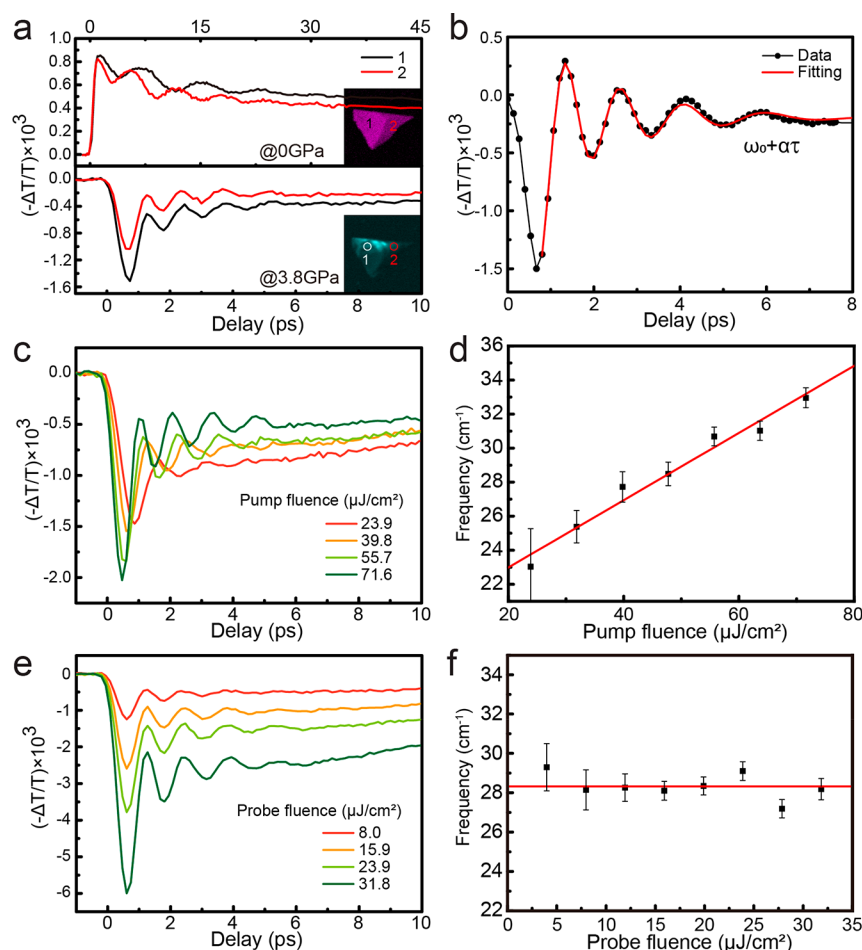
Figure 4. TAM coherent phonon properties in the semimetal phase. (a) LAM and TAM phonon dynamics resolved in two different regions, showing strong thickness-dependence of the LAM and the thickness-independence of the TAM phonons. (b) Time-resolved "phonon-chirping" of the TAM phonon. (c,d) Stiffening of TAM phonon with increasing pump power (fixed probe fluence of 11.9 μJ/cm^2). (e,f) Independence of TAM phonon frequency on probe power (fixed pump fluence: 47.7 μJ/cm^2).

dependence as sample gets thicker ($N > 15$ in this study).[40] Phonon softening with increased pressure and decreased carrier density under the Sm-BP phase indicate connections between TAM phonons and nonequilibrium carriers.[42,43]

To further elucidate the appreciable pressure-driven phonon softening, we implement density functional theory to calculate the geometry of BP, the corresponding electronic band structure and phonon spectra under different compressive strains (supplementary Note and Figure S8). To better characterize the shear mode, all calculations are performed with the conventional cell of orthorhombic BP (Figure 5a). We optimized the geometry with different uniaxial compressive strains (CS, ε_{zz}). Our calculations have shown a notable contraction of the interlayer distance as the CS increases. When the CS reaches 12.5%, the interlayer distance in BP decreases from 3.05A to 2.45A. To further expose the underlying mechanism, we employed density functional perturbation theory (DFPT) in linear response to calculate the evolution of phonon dispersion relations with excess CS. As shown in Figure 5b, the orthorhombic phase maintains stable under 0−11.25% CS. The phonon frequency of a specific TAM mode along Γ-Z gradually decreases with increasing CS and comes to a complete imaginary frequency at 12.5% CS. Analysis of the phonon eigenvector indicates that the softening mode corresponds to shearing along the armchair

orientation (Figure 5c). In contrast, the shear mode along the zigzag orientation shows little variation with a varying CS.

We performed EPC calculations to gain further insights into how CS affects the shear mode evolution. As shown in Figure 5b, the EPC of shear mode along the armchair orientation mode is negligible at 0% CS and receives overall enhancement with increasing CS, which explains the absence of TAM mode at the low-pressure region. Particularly noteworthy is the significant enhancement of the EPC for the TAM mode at a specific q-point along Γ-Z, coinciding with a substantial decrease in the phonon frequency. The coherent electron−phonon coupling enhancement and phonon softening can explain the observed phonon softening in Figure 3f. Interestingly, when the CS reaches 12.5%, the TAM mode at the same q-point becomes imaginary, while the frequency at the Γ-point remains real. Both observations indicate that a supercell lattice reconstruction will occur under the CS.

The strength of CP oscillation is primarily determined by the coupling between the dielectric constant and lattice motions. Both LAM and TAM CPs are potentially excited simultaneously, exerting a dominant influence on modulating the dielectric constant and TA signal in two distinct electronic phases, i.e., Sc-BP and Sm-BP phases, which reflect the competitive coupling between acoustic phonons and non-equilibrium carriers under varying pressure conditions. Our
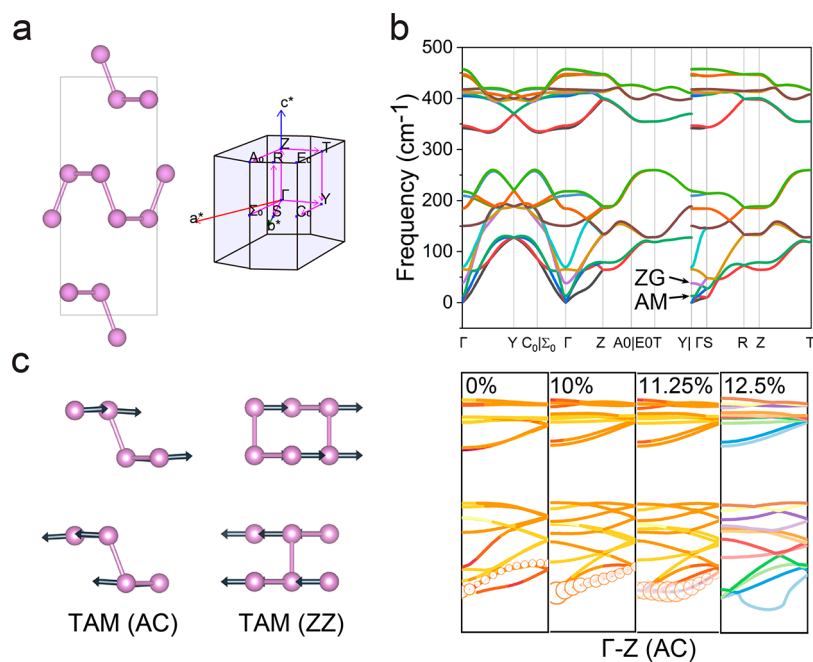
Figure 5. DFT calculations of pressure-driven coherent phonon softening and enhanced electron−phonon coupling. (a) Crystal structure of bulk BP conventional cell and the Brillouin zone path of BP primitive cell. (b) Full phonon dispersion for bulk BP conventional cell (upper panel). Phonon dispersion along the AC direction under different uniaxial compressive strains (lower panel). The color scheme in the lower panel corresponds to the q-resolved EPC parameter. And the size of the circle indicates the strength of the EPC parameter size of the specific TAM mode. (c) Eigenvectors of the shearing TAM.

calculations confirm that increasing pressure either weakens the EPC strength of LAM or enhances that of TAM, thus leading to a diminished LAM CP and a softening of TAM CP. On the other hand, ultrafast laser excitation also significantly alters the phonon frequency through modified EPC strength. The hardening of the TAM phonon induced by increasing pump power implied that e-ph interaction plays a dominant role. In our case, the photoexcited carriers raise the Fermi level and hinder the effective relaxation of phonons into e-h pairs, resulting in a weakened EPC strength. Similar phonon stiffening has been observed in semimetallic materials (for instance graphene/graphite) by adjusting the Fermi level through electric tuning or laser excitation, thus regulating the strength of EPC.[42−44] Note the frequency of LAM phonon in Sc-BP phase is pump-power independent (Figure S9), which could be attributed to weak EPC strength.

The pressure induced softening behavior of TAM may indicate lattice instability that correlates with structural phase transition since a decrease in phonon frequency signifies a reduced restoring force of lattice vibration, potentially leading to symmetry broken. While in the case of a phase transition, the direction of the restoring force is reversed, and the phonon frequency turns to a negative number. Nonequilibrium carriers always play an important role in structural distortion by altering atomic vibrations, and phonon softening modified by EPC was observed in other system with similar behaviors, such as Kohn anomaly in graphite and soft phonon mode in ferroelectric phase transitions.[45,46] Moreover, modulating EPC strength was also reported as significant in charge density wave (CDW), ferroelectric and superconducting transitions.[47−49] Our results demonstrated pressure and nonequilibrium carrier density as two important factors in modulating EPC.

Our current pump−probe microscopy apparatus could be further improved to excite/detect resonant excitonic tran-

sitions in few-layer BP under high pressures. To do so, it would be better to make the tunable-wavelength laser beam the pump and the fixed beam the probe. Frequency-doubling may also be needed to shift the wavelengths to the visible range for larger bandgap materials such as single-layer BP. Moreover, supersolution techniques could be applied to improve spatial resolution of pump−probe type microscopy by implementing stimulated-emission-depletion (STED)-like techniques.[50,51]

In summary, we have systematically investigated the ultrafast carrier and coherent phonon dynamics during phase transitions of BP films within ∼22 GPa using high-pressure-compatible femtosecond pump−probe microscopy. The spatially resolved ultrafast TA images and carrier dynamics directly revealed the pressure induced modifications of the electronic structure (Sc-BP to Sm-BP) and lattice structure (BP- BlueP-SC phases). We found a common hardening of LAM phonons in the semiconductor phase and an anomalous softening of TAM phonons in the semimetal phase. Furthermore, we demonstrated carrier-density and time dependences of TAM frequency and revealed peculiar electron−phonon coupling, as verified by DFT calculations. Our results offer valuable insights for the modulation of band gap, lattice structure, and EPC strength with pressure.

■ ASSOCIATED CONTENT

Ⓢ Supporting Information

The Supporting Information is available free of charge at https://pubs.acs.org/doi/10.1021/acs.nanolett.3c04218.

> Experimental methods; spatial resolution characterization and polarization response of high-pressure microscope system; high-pressure Raman spectra; amplitude and damping-time evolution of LAM; coherent phonons in a 9 nm-thick sample; wavelength-dependence of TAM oscillation; calculated phonon

spectra; and phonon frequency dependence on laser power (PDF)

Movie S1: pump−probe imaging with varying pressures (MP4)

AUTHOR INFORMATION

Corresponding Authors

Minbiao Ji − *State Key Laboratory of Surface Physics and Department of Physics, Key Laboratory of Micro and Nano Photonic Structures (Ministry of Education), Shanghai Key Laboratory of Metasurfaces for Light Manipulation, Fudan University, Shanghai 200433, China; Academy for Engineering and Technology, Yiwu Research Institute of Fudan University, Fudan University, Shanghai 200433, China;* orcid.org/0000-0002-9066-4008; Email: minbiaoj@fudan.edu.cn

Yang Lu − *Center for High Pressure Science & Technology Advanced Research, Shanghai 201203, China; Shanghai Key Laboratory of Material Frontiers Research in Extreme Environments (MFree), Shanghai Advanced Research in Physical Sciences (SHARPS), Shanghai 201203, China;* orcid.org/0000-0003-4000-712X; Email: yang.lu@hpstar.ac.cn

Weibin Chu − *State Key Laboratory of Surface Physics and Department of Physics, Key Laboratory of Micro and Nano Photonic Structures (Ministry of Education), Shanghai Key Laboratory of Metasurfaces for Light Manipulation, Fudan University, Shanghai 200433, China; Key Laboratory of Computational Physical Science (MOE) and Institute of Computational Physical Science, Fudan University, Shanghai 200433, China;* orcid.org/0000-0001-5951-0337; Email: wbchu@fudan.edu.cn

Author

Simin Wu − *State Key Laboratory of Surface Physics and Department of Physics, Key Laboratory of Micro and Nano Photonic Structures (Ministry of Education), Shanghai Key Laboratory of Metasurfaces for Light Manipulation, Fudan University, Shanghai 200433, China;* orcid.org/0009-0008-7007-6613

Complete contact information is available at:
https://pubs.acs.org/10.1021/acs.nanolett.3c04218

Author Contributions

S.W. and W.C. contributed equally. M.J. and S.M. designed the experiments, S.M. prepared the samples and performed the pump−probe microscopy measurements, Y.L. helped with DAC operations, W.C. conducted the DFPT calculations. The manuscript was written by S.W., M.J. and W.C. and revised by all authors. All authors have given approval to the final version of the manuscript.

Notes

The authors declare no competing financial interest.

REFERENCES

(1) Li, L.; Kim, J.; Jin, C.; Ye, G. J.; Qiu, D. Y.; da Jornada, F. H.; Shi, Z.; Chen, L.; Zhang, Z.; Yang, F.; Watanabe, K.; Taniguchi, T.; Ren, W.; Louie, S. G.; Chen, X. H.; Zhang, Y.; Wang, F. Direct Observation of the Layer-Dependent Electronic Structure in Phosphorene. *Nat. Nanotechnol.* **2017**, *12* (1), 21−25.

(2) Zhang, G.; Huang, S.; Chaves, A.; Song, C.; Özçelik, V. O.; Low, T.; Yan, H. Infrared Fingerprints of Few-Layer Black Phosphorus. *Nat. Commun.* **2017**, *8* (1), 14071.

(3) Miao, X.; Zhang, G.; Wang, F.; Yan, H.; Ji, M. Layer-Dependent Ultrafast Carrier and Coherent Phonon Dynamics in Black Phosphorus. *Nano Lett.* **2018**, *18* (5), 3053−3059.

(4) Ling, X.; Huang, S.; Hasdeo, E. H.; Liang, L.; Parkin, W. M.; Tatsumi, Y.; Nugraha, A. R. T.; Puretzky, A. A.; Das, P. M.; Sumpter, B. G.; Geohegan, D. B.; Kong, J.; Saito, R.; Drndic, M.; Meunier, V.; Dresselhaus, M. S. Anisotropic Electron-Photon and Electron-Phonon Interactions in Black Phosphorus. *Nano Lett.* **2016**, *16* (4), 2260−2267.

(5) Jang, H.; Wood, J. D.; Ryder, C. R.; Hersam, M. C.; Cahill, D. G. Anisotropic Thermal Conductivity of Exfoliated Black Phosphorus. *Adv. Mater.* **2015**, *27* (48), 8017−8022.

(6) Wang, F.; Wang, C.; Chaves, A.; Song, C.; Zhang, G.; Huang, S.; Lei, Y.; Xing, Q.; Mu, L.; Xie, Y.; Yan, H. Prediction of Hyperbolic Exciton-Polaritons in Monolayer Black Phosphorus. *Nat. Commun.* **2021**, *12* (1), 5628.

(7) Zhang, G.; Huang, S.; Wang, F.; Yan, H. Layer-Dependent Electronic and Optical Properties of 2D Black Phosphorus: Fundamentals and Engineering. *Laser & Photonics Reviews* **2021**, *15* (6), 2000399.

(8) Huang, S.; Zhang, G.; Fan, F.; Song, C.; Wang, F.; Xing, Q.; Wang, C.; Wu, H.; Yan, H. Strain-Tunable van Der Waals Interactions in Few-Layer Black Phosphorus. *Nat. Commun.* **2019**, *10* (1), 2447.

(9) Deng, B.; Tran, V.; Xie, Y.; Jiang, H.; Li, C.; Guo, Q.; Wang, X.; Tian, H.; Koester, S. J.; Wang, H.; Cha, J. J.; Xia, Q.; Yang, L.; Xia, F. Efficient Electrical Control of Thin-Film Black Phosphorus Bandgap. *Nat. Commun.* **2017**, *8* (1), 14474.

(10) Liu, Y.; Rodrigues, J. N. B.; Luo, Y. Z.; Li, L.; Carvalho, A.; Yang, M.; Laksono, E.; Lu, J.; Bao, Y.; Xu, H.; Tan, S. J. R.; Qiu, Z.; Sow, C. H.; Feng, Y. P.; Neto, A. H. C.; Adam, S.; Lu, J.; Loh, K. P. Tailoring Sample-Wide Pseudo-Magnetic Fields on a Graphene-Black Phosphorus Heterostructure. *Nat. Nanotechnol.* **2018**, *13* (9), 828−834.

(11) Zong, X.; Hu, H.; Ouyang, G.; Wang, J.; Shi, R.; Zhang, L.; Zeng, Q.; Zhu, C.; Chen, S.; Cheng, C.; Wang, B.; Zhang, H.; Liu, Z.; Huang, W.; Wang, T.; Wang, L.; Chen, X. Black Phosphorus-Based van Der Waals Heterostructures for Mid-Infrared Light-Emission Applications. *Light Sci. Appl.* **2020**, *9* (1), 114.

(12) Yang, Z.; Hao, J. Recent Progress in Black-Phosphorus-Based Heterostructures for Device Applications. *Small Methods* **2018**, *2* (2), 1700296.

(13) Pei, S.; Wang, Z.; Xia, J. High Pressure Studies of 2D Materials and Heterostructures: A Review. *Materials & Design* **2022**, *213*, 110363.

(14) Zhang, L.; Tang, Y.; Khan, A. R.; Hasan, M. M.; Wang, P.; Yan, H.; Yildirim, T.; Torres, J. F.; Neupane, G. P.; Zhang, Y.; Li, Q.; Lu, Y. 2D Materials and Heterostructures at Extreme Pressure. *Advanced Science* **2020**, *7* (24), 2002697.

(15) Gupta, S. N.; Singh, A.; Pal, K.; Chakraborti, B.; Muthu, D. V. S.; Waghmare, U. V.; Sood, A. K. Raman Anomalies as Signatures of Pressure Induced Electronic Topological and Structural Transitions in Black Phosphorus: Experiments and Theory. *Phys. Rev. B* **2017**, *96* (9), 094104.

(16) Chi, Z.; Chen, X.; Yen, F.; Peng, F.; Zhou, Y.; Zhu, J.; Zhang, Y.; Liu, X.; Lin, C.; Chu, S.; Li, Y.; Zhao, J.; Kagayama, T.; Ma, Y.;

Yang, Z. Superconductivity in Pristine 2Ha-MoS$_2$ at Ultrahigh Pressure. *Phys. Rev. Lett.* **2018**, *120* (3), 037002.

(17) Wang, Y.; Ying, J.; Zhou, Z.; Sun, J.; Wen, T.; Zhou, Y.; Li, N.; Zhang, Q.; Han, F.; Xiao, Y.; Chow, P.; Yang, W.; Struzhkin, V. V.; Zhao, Y.; Mao, H. Emergent Superconductivity in an Iron-Based Honeycomb Lattice Initiated by Pressure-Driven Spin-Crossover. *Nat. Commun.* **2018**, *9* (1), 1914.

(18) Ke, F.; Chen, Y.; Yin, K.; Yan, J.; Zhang, H.; Liu, Z.; Tse, J. S.; Wu, J.; Mao, H.; Chen, B. Large Bandgap of Pressurized Trilayer Graphene. *Proc. Natl. Acad. Sci. U.S.A.* **2019**, *116* (19), 9186−9190.

(19) Bai, L.; Li, Q.; Corr, S. A.; Meng, Y.; Park, C.; Sinogeikin, S. V.; Ko, C.; Wu, J.; Shen, G. Pressure-Induced Phase Transitions and Metallization in VO$_2$. *Phys. Rev. B* **2015**, *91* (10), 104110.

(20) O'Callahan, B. T.; Jones, A. C.; Hyung Park, J.; Cobden, D. H.; Atkin, J. M.; Raschke, M. B. Inhomogeneity of the Ultrafast Insulator-to-Metal Transition Dynamics of VO$_2$. *Nat. Commun.* **2015**, *6* (1), 6849.

(21) Nayak, A. P.; Yuan, Z.; Cao, B.; Liu, J.; Wu, J.; Moran, S. T.; Li, T.; Akinwande, D.; Jin, C.; Lin, J.-F. Pressure-Modulated Conductivity, Carrier Density, and Mobility of Multilayered Tungsten Disulfide. *ACS Nano* **2015**, *9* (9), 9117−9123.

(22) Xiang, Z. J.; Ye, G. J.; Shang, C.; Lei, B.; Wang, N. Z.; Yang, K. S.; Liu, D. Y.; Meng, F. B.; Luo, X. G.; Zou, L. J.; Sun, Z.; Zhang, Y.; Chen, X. H. Pressure-Induced Electronic Transition in Black Phosphorus. *Phys. Rev. Lett.* **2015**, *115* (18), 186403.

(23) Vanderborgh, C. A.; Schiferl, D. Raman Studies of Black Phosphorus from 0.25 to 7.7 GPa at 15 K. *Phys. Rev. B* **1989**, *40* (14), 9595−9599.

(24) Akahama, Y.; Kobayashi, M.; Kawamura, H. Raman Study of Black Phosphorus up to 13 GPa. *Solid State Commun.* **1997**, *104* (6), 311−315.

(25) Kundu, A.; Tristant, D.; Sheremetyeva, N.; Yoshimura, A.; Torres Dias, A.; Hazra, K. S.; Meunier, V.; Puech, P. Reversible Pressure-Induced Partial Phase Transition in Few-Layer Black Phosphorus. *Nano Lett.* **2020**, *20* (8), 5929−5935.

(26) Li, Q.; Huang, H.; Chen, Z.; Huang, X.; Deng, K.; Luo, S.; Wang, Z.; Yu, X.; Quan, Z. Thickness-Dependent Structural Stability and Anisotropy of Black Phosphorus. *Advanced Electronic Materials* **2019**, *5* (3), 1800712.

(27) Huang, S.; Lu, Y.; Wang, F.; Lei, Y.; Song, C.; Zhang, J.; Xing, Q.; Wang, C.; Xie, Y.; Mu, L.; Zhang, G.; Yan, H.; Chen, B.; Yan, H. Layer-Dependent Pressure Effect on the Electronic Structure of 2D Black Phosphorus. *Phys. Rev. Lett.* **2021**, *127* (18), 186401.

(28) Chen, Z.; Dong, J.; Papalazarou, E.; Marsi, M.; Giorgetti, C.; Zhang, Z.; Tian, B.; Rueff, J.-P.; Taleb-Ibrahimi, A.; Perfetti, L. Band Gap Renormalization, Carrier Multiplication, and Stark Broadening in Photoexcited Black Phosphorus. *Nano Lett.* **2019**, *19* (1), 488−493.

(29) Wu, S.; Lu, Z.; Hu, A.; Miao, X.; Wang, F.; Sun, Z.; Yan, H.; Zhang, H.; Ji, M. Dichroic Photoelasticity in Black Phosphorus Revealed by Ultrafast Coherent Phonon Dynamics. *J. Phys. Chem. Lett.* **2021**, *12* (25), 5871−5878.

(30) Zhu, Y.; Cheng, J.-X. Transient Absorption Microscopy: Technological Innovations and Applications in Materials Science and Life Science. *J. Chem. Phys.* **2020**, *152* (2), 020901.

(31) Matthews, T. E.; Piletic, I. R.; Selim, M. A.; Simpson, M. J.; Warren, W. S. Pump-Probe Imaging Differentiates Melanoma from Melanocytic Nevi. *Sci. Transl. Med.* **2011**, *3* (71), 71ra15.

(32) Zhang, L.; Zou, X.; Zhang, B.; Cui, L.; Zhang, J.; Mao, Y.; Chen, L.; Ji, M. Label-Free Imaging of Hemoglobin Degradation and Hemosiderin Formation in Brain Tissues with Femtosecond Pump-Probe Microscopy. *Theranostics* **2018**, *8* (15), 4129−4140.

(33) Zhang, B.; Yao, T.; Chen, Y.; Wang, C.; Bao, Y.; Wang, Z.; Zhao, K.; Ji, M. Label-Free Delineation of Human Uveal Melanoma Infiltration With Pump-Probe Microscopy. *Front. Oncol.* **2022**, *12*, 891282.

(34) Chen, Y.; Wang, R.; Ji, M. Nondestructive Nonlinear Optical Microscopy Revealed the Blackening Mechanism of Ancient Chinese Jades. *Research* **2023**, *6*, 0266.

(35) Mao, H. K.; Bell, P. M.; Shaner, J. W.; Steinberg, D. J. Specific Volume Measurements of Cu, Mo, Pd, and Ag and Calibration of the Ruby R1 Fluorescence Pressure Gauge from 0.06 to 1 Mbar. *J. Appl. Phys.* **1978**, *49* (6), 3276−3283.

(36) Forman, R. A.; Piermarini, G. J.; Barnett, J. D.; Block, S. Pressure Measurement Made by the Utilization of Ruby Sharp-Line Luminescence. *Science* **1972**, *176* (4032), 284−285.

(37) Tian, Z. Y.; Zhang, Q. Y.; Xiao, Y. W.; Gamage, G. A.; Tian, F.; Yue, S.; Hadjiev, V. G.; Bao, J.; Ren, Z.; Liang, E.; Zhao, J. Ultraweak Electron-Phonon Coupling Strength in Cubic Boron Arsenide Unveiled by Ultrafast Dynamics. *Phys. Rev. B* **2022**, *105* (17), 174306.

(38) Meng, S.; Shi, H.; Jiang, H.; Sun, X.; Gao, B. Anisotropic Charge Carrier and Coherent Acoustic Phonon Dynamics of Black Phosphorus Studied by Transient Absorption Microscopy. *J. Phys. Chem. C* **2019**, *123* (32), 20051−20058.

(39) Hu, Z.-X.; Kong, X.; Qiao, J.; Normand, B.; Ji, W. Interlayer Electronic Hybridization Leads to Exceptional Thickness-Dependent Vibrational Properties in Few-Layer Black Phosphorus. *Nanoscale* **2016**, *8* (5), 2740−2750.

(40) Jiang, J.-W.; Wang, B.-S.; Park, H. S. Interlayer Breathing and Shear Modes in Few-Layer Black Phosphorus. *J. Phys.: Condens. Matter* **2016**, *28* (16), 165401.

(41) Appalakondaiah, S.; Vaitheeswaran, G.; Lebègue, S.; Christensen, N. E.; Svane, A. Effect of van Der Waals Interactions on the Structural and Elastic Properties of Black Phosphorus. *Phys. Rev. B* **2012**, *86* (3), 035105.

(42) Yan, H.; Song, D.; Mak, K. F.; Chatzakis, I.; Maultzsch, J.; Heinz, T. F. Time-Resolved Raman Spectroscopy of Optical Phonons in Graphite: Phonon Anharmonic Coupling and Anomalous Stiffening. *Phys. Rev. B* **2009**, *80* (12), 121403.

(43) Ferrante, C.; Virga, A.; Benfatto, L.; Martinati, M.; De Fazio, D.; Sassi, U.; Fasolato, C.; Ott, A. K.; Postorino, P.; Yoon, D.; Cerullo, G.; Mauri, F.; Ferrari, A. C.; Scopigno, T. Raman Spectroscopy of Graphene under Ultrafast Laser Excitation. *Nat. Commun.* **2018**, *9* (1), 308.

(44) Yan, J.; Zhang, Y.; Kim, P.; Pinczuk, A. Electric Field Effect Tuning of Electron-Phonon Coupling in Graphene. *Phys. Rev. Lett.* **2007**, *98* (16), 166802.

(45) Piscanec, S.; Lazzeri, M.; Mauri, F.; Ferrari, A. C.; Robertson, J. Kohn Anomalies and Electron-Phonon Interactions in Graphite. *Phys. Rev. Lett.* **2004**, *93* (18), 185503.

(46) Kamba, S. Soft-Mode Spectroscopy of Ferroelectrics and Multiferroics: A Review. *APL Materials* **2021**, *9*, 020704.

(47) Ma, J.; Yang, R.; Chen, H. A Large Modulation of Electron-Phonon Coupling and an Emergent Superconducting Dome in Doped Strong Ferroelectrics. *Nat. Commun.* **2021**, *12* (1), 2314.

(48) Cheng, C.; Sun, J.-T.; Liu, M.; Chen, X.-R.; Meng, S. Tunable Electron-Phonon Coupling Superconductivity in Platinum Diselenide. *Phys. Rev. Materials* **2017**, *1* (7), 074804.

(49) Peng, Y. Y.; Husain, A. A.; Mitrano, M.; Sun, S. X.-L.; Johnson, T. A.; Zakrzewski, A. V.; MacDougall, G. J.; Barbour, A.; Jarrige, I.; Bisogni, V.; Abbamonte, P. Enhanced Electron-Phonon Coupling for Charge-Density-Wave Formation in La$_{1.8-x}$Eu$_{0.2}$Sr$_x$CuO$_{4+\delta}$. *Phys. Rev. Lett.* **2020**, *125* (9), 097002.

(50) Wang, P.; Slipchenko, M. N.; Mitchell, J.; Yang, C.; Potma, E. O.; Xu, X.; Cheng, J.-X. Far-Field Imaging of Non-Fluorescent Species with Subdiffraction Resolution. *Nature Photon* **2013**, *7* (6), 449−453.

(51) Ao, J.; Fang, X.; Ma, L.; Liu, Z.; Wu, S.; Wu, C.; Ji, M. Photoswitchable Vibrational Nanoscopy with Sub-100-Nm Optical Resolution. *Adv. Photon.* **2023**, *5* (06), 066001.